Journal of Manufacturing Processes 139 (2025) 210–223

Contents lists available at ScienceDirect

Journal of Manufacturing Processes

journal homepage: www.elsevier.com/locate/manpro

Comprehensive analysis of the forming zone and improvement of diameter reduction prediction in the dieless wire drawing process

Merle Braatz [a,*], Jan Bohlen [a], Noomane Ben Khalifa [a,b]

[a] Institute of Material and Process Design, Helmholtz-Zentrum Hereon, Max-Planck-Straße 1, 21502 Geesthacht, Germany
[b] Institute for Production Technology and Systems, Leuphana Universität Lüneburg, Universitätsallee 1, 21335 Lüneburg, Germany

ARTICLE INFO

Keywords:
Plastic deformation
Dieless wire drawing
Forming zone
Hot forming
Magnesium alloy

ABSTRACT

The main disadvantage of the dieless wire drawing process is the complex interdependence of the process parameters, which often leads to process instability. The objective of this paper is to integrate the analysis of material behaviour with process performance, thereby extending the range of applicability and enhancing process control. For this purpose, the forming zone and its length are investigated and evaluated in detail to identify stable process scenarios and to predict the occurrence of (non-)localised deformation and actual diameter reduction. It is found that elevated temperatures above about 0.6 times the melting temperature result in well localised deformation, whereas increasing the feeding speed or the reduction ratio increases the length of the forming zone. An equation is presented for calculating the length of the forming zone based on material properties and process settings. In addition, stable process conditions are given, including minimum forming zone lengths and maximum possible diameter reductions. Predictions of actual diameter reductions using different approaches are also presented.

1. Introduction

Developed in the 1960s [1], the dieless wire drawing (DD) process aims to increase productivity by enabling greater reduction in cross-sectional area (CSA) and hot forming processes without subsequent or intermediate heat treatments. By eliminating the need for (multiple) forming tools, the process became more flexible, allowing for greater diameter reduction, continuously adjustable final diameters and diameter changes during the process. This flexibility also extended to the production of tapered bar shapes [2,3], piecewise linear diameter contours [4], other CSA shapes [5,6] and hollow structures such as microtubes [7,8]. Despite these advantages, multiple passes are still required to improve processability [9] and stability [10] to achieve thin final diameters. Another method of producing thin wires is to start with smaller diameter starting material, e.g. directly extruded wires with diameters as small as 0.2 mm [11].

However, the DD process has not yet been industrialised due to several significant challenges. The complex interdependence of process parameters [12], the decreasing uniformity of wire diameter as the reduction ratio increases [13], and the likely non-uniformity of diameter along the wire [14] have all contributed to process instability. This instability has been the main reason for the commercial failure of the DD process [15], although it remains of interest for specialised applications such as sutures [16] or stents [17] for medical purposes, particularly with biodegradable materials such as magnesium or zinc.

The forming zone is the area of the wire where deformation occurs during processing as a result of localised heating. The length of this area is defined as the forming zone length l_{fz} (see Fig. 1). Since there is no drawing die that defines the geometry of the deformation zone from the outside, the deformation of the wire in the DD process depends solely on the process parameters, in particular on the temperature and stress development along the length of the wire. This makes the process very susceptible to instability. In early studies, the sensitivity of the DD process [12], the development of a steady state [18] and the process stability [15] are described. Process stability is defined as the absence of wire fracture, only small diameter variations in the process steady state and small to no differences between set analytical and the resulting experimental CSA reduction values. A good understanding of the process variables and their influence on the forming zone is thus essential to achieve and control a stable and accurate process.

Researchers have addressed these challenges in various ways. Fortunier et al. in [19] and Pawelski and Knollig in [20] identify the

* Corresponding author.
E-mail address: merle.braatz@hereon.de (M. Braatz).

https://doi.org/10.1016/j.jmapro.2025.02.035
Received 12 September 2024; Received in revised form 4 February 2025; Accepted 13 February 2025
Available online 18 February 2025

forming zone indirectly by analysing and calculating the temperature profile. Weidig and Steinhoff in [21,22], followed by Tiernan and Hillery in [13], describe the forming zone by analysing the temperature and yield stress development over the wire length for steel wires. Thereby, Weidig and Steinhoff define in [22] the forming zone from the point of maximum temperature to the point at which the temperature-dependent yield strength of the material becomes greater than the tensile stress. Tiernan et al. provide in [12] an equation adapted to the DD process for calculating the forming zone length, whereby this equation requires knowledge of the strain rate and they calculate the strain rate based on the geometry of the cold wire drawing linear deformation profile. Braatz et al. investigate in [23] the forming zone and its changes due to process parameter variations using finite element methods, while Hongyu et al. analyse the deformation using a vertical gradient slap method [24]. He et al. use in [25] machine vision and an online control system to control and adjust diameter changes during DD experiments by controlling the deformation zone. In previous work by these authors [26], the length of the forming zone is measured at steady state. It is also demonstrated that the position of the deformation and the length of the forming zone have direct effects on the resulting final diameter, process window and process stability [26]. However, apart from in-process measurements, all existing studies use unknown parameters or require numerical or finite element methods to calculate the forming zone length. The forming zone length is crucial for ensuring process stability in the DD process, because a stable and well-defined forming zone ensures consistent and uniform deformation. The evolution of the forming zone length in the mathematical model of the DD process, particularly in the forming zone, results in a quantity that is dependent on yield stress, temperature and strain rate [13]. This characteristic allows direct assessment of material processing effects during DD. Calculating the forming zone length through numerical methods and experimental validation is essential for achieving these goals.

The objective of this paper is to integrate the analysis of material behaviour with process performance, thereby extending the range of applicability and enhancing process control. For this purpose, the forming zone and its length are investigated and evaluated in detail to identify stable deformation scenarios and to predict the occurrence of (non-)localised deformation and actual diameter reduction.

2. Materials and experiments

The starting material for the DD experiments are directly extruded ZX10 (Mg-1%Zn- 0.15%Ca) wires with 1 mm diameter. This alloy and its series received some attention as a highly formable wrought magnesium alloy due to the inclusion of calcium as an alloying element and the concurrent microstructure development features during processing [27]. In addition, aluminium-free magnesium alloys such as ZX10 are of increasing interest for biodegradable implant materials, e.g. as suture material, as a starting material for stents or support meshes [17,28]. Therefore, ZX10 wires are chosen as the starting material for this work because of their comparatively good formability among magnesium alloys and their potential application as biodegradable wires. The wires are extruded from a 150 x Ø49 mm billet through a 4 × 1 mm die at 400 °C and a ram speed of 0.2 mm/s. Details of the casting and the extrusion of the material can be found in Nienaber et al. in [29].

In this study, a continuous DD process is used (see Fig. 1). In this setup, the wire moves at a feeding speed v_0 and a higher drawing speed v_1. The wire is locally heated by an induction coil and is then passively cooled by air, allowing a plastic deformation zone where the wire diameter reduces from the initial CSA A_0 to the final CSA A_1. Based on the volume consistency relation, the ideal CSA reduction R_{ideal} based on the induced force for deformation is determined using the relation between the wire's CSAs and the process speeds:

$$R_{ideal} := 1 - \frac{v_0}{v_1} = 1 - \frac{A_1}{A_0} \tag{1}$$

In earlier work Braatz et al. [26] observe a discrepancy between the two sides of the equation in (1) and therefore propose to distinguish between the analytical CSA reduction ratio R_{an} and the experimental CSA reduction ratio R_{exp}. However, given the volume consistency, this discrepancy between the two values should not exist which will be discussed later in section 4. There, a correction factor η will be introduced to describe the mentioned discrepancy between the CSA reduction ratios:

$$\eta\, R_{an} = R_{exp} \tag{2}$$

Based on the law of volume constancy the CSA reduction R can thus be determined in advance by the set process speeds (analytical) or after the drawing pass by the wire diameters, respective CSAs, before and after the DD process (experimental):

$$\text{Analytical} : R_{an} = 1 - \frac{v_0}{v_1} \text{ and} \tag{3}$$

$$\text{Experimental} : R_{exp} = 1 - \frac{A_1}{A_0} \tag{4}$$

For the DD experiments, a flexible wire drawing setup described in previous work [26] is used. The wires are drawn at a range of temperatures (50, 150, 250, 350, 420 °C), feeding speeds (5, 10, 20 mm/s) and CSA reductions (10, 20, 30 %) with a total of 45 experiments performed. At the begin of each experiment, the induction heating and the wire spool speeds are started simultaneously. Since the starting conditions of the experimental setup do not influence the length of the forming zone in the steady state, they are kept the same for all experiments and are chosen so that an instant start and stop of the process is ensured with an

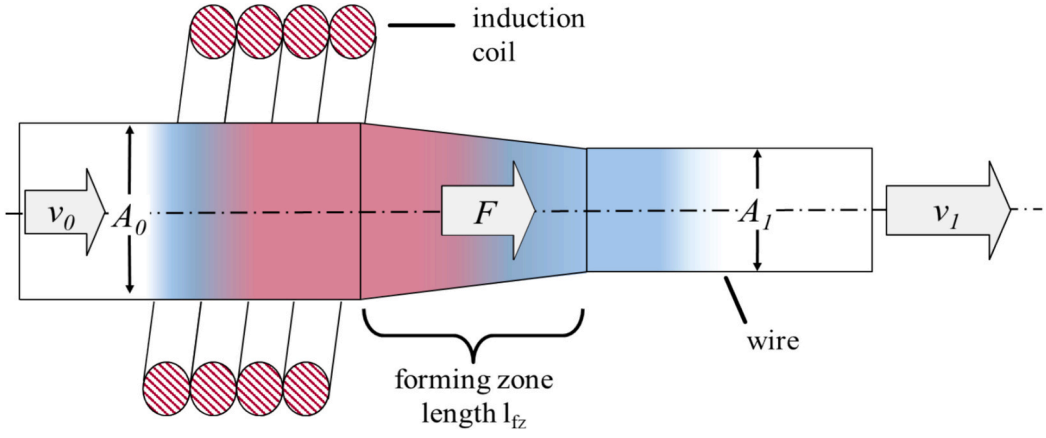

Fig. 1. Schematic illustration of the dieless wire drawing process.

acceleration of 1000 mm/s^2. Each experiment results in a wire of approx. 2.5 m in length and during each experiment, the process tensile forces and the diameter measurements are exported. In order to measure the length of the forming zone l_{fz} in the steady state of the process, at the end of each experiment the drawing speed v_1 is set to the feeding speed v_0 in order to remove the applied force, while at the same time the heating by the induction coil is switched off. While the wire continues to move, the length of the forming zone l_{fz} can be recorded by means of diameter measurements. After the experiment, the wire position of the diameter measurements is corrected by the distance from the end of the induction coil to the laser measuring point, as the laser device is placed at a distance from the induction coil due to its electronics and the limited installation space.

Tensile tests are carried out to determine the material parameters using a Zwick universal testing machine with a maximum load of 5 kN at 50, 150 and 250 °C and with strain rates of 0.001, 0.01 and 0.1/s. A minimum of five samples with a gauge length of 50 mm are tested for each condition. The obtained engineering strain-stress curves are then converted to true strain-stress curves using standard transformation eqs. (5) and (6) and the peak stresses are then used for further data processing:

$$\sigma_{true} = \sigma_{eng}\left(1+\varepsilon_{eng}\right), \text{and} \tag{5}$$

$$\varepsilon_{true} = ln\left(1+\varepsilon_{eng}\right) \tag{6}$$

3. Forming zone during dieless wire drawing

The forming zone is the region where the wire undergoes significant plastic deformation. As can be seen in Fig. 1, the forming zone length l_{fz} is defined as the region in which the wire deforms: the wire diameter changes from the initial diameter d_0 of the as-extruded wire to the final diameter d_1 of the drawn wire. In the DD process, the length and the geometry of the forming zone is not predetermined by a tool. This means that its evolution and the profile of the forming zone depend only on the process parameters and the material's response to the independent process parameters of temperature and speed, respectively, and therefore on the evolution of a localised deformation in the steady state of the process. Among the independent process parameters, the temperature is the main control parameter as it can be influenced locally by heating (and active cooling if implemented), whereas the speed difference v_0/v_1, which enforces the CSA reduction, can only be controlled globally between the two wire spools used.

In order to analyse the forming zone and its dependence on the process parameters, a separation of the effects by changing one parameter at a time is investigated. To do this, the diameter and force measurements over the process time for different temperatures, diameter reductions and feeding speeds are compared in Fig. 2, Fig. 3 and Fig. 4 respectively. Any gaps in the line graphs are due to reference spray paint points on the wire to calibrate the temperature measurements.

3.1. Influence of the temperature

Fig. 2 shows the diameter measurements in grey and the force measurements in red over the wire length for (a) 50 °C and (b) 350 °C wire temperature. Both experiments are carried out with a feeding speed of 10 mm/s and with a set CSA reduction of 20 %.

In both graphs, the wire diameter initially decreases with a slope until the final diameter d_1 is reached. This distance is coloured as light grey area and marks the transition zone. During these first seconds, the DD process transitions from an unstable phase to its stable steady state. Its length depends on the start-up conditions of the experiment which are kept constant for this study as no effect on the deformation and the forming zone length as steady state properties of the process are assumed. At the end of the experiment, the tensile force is removed, and the heating is switched off for both graphs as described in the experiment section to measure the forming zone length in the steady state. The distance from the established final diameter d_1 in the steady state back to the initial (as-extruded) diameter d_0 is coloured as light blue zone and marks the forming zone l_{fz}. The zone between the grey and blue areas represents the deformed wire and its length will only change when the experiment time is varied. In this zone, the process is in its steady state where the process forces, temperatures and material reactions are in equilibrium and the forming zone is established.

For the experiment carried out at 50 °C, the system takes longer to reach its stable steady state and the forming zone is 582 mm long. A significant increasing in temperature to 350 °C results in a much shorter transition zone and forming zone (82 mm). Instead of a slowly decreasing diameter, the diameter changes are more abrupt, and the system takes less time reach its steady state. The deformation is more localised, and the graph shows a diameter undershoot at the end of the transition zone. The process force at 50 °C increases at the beginning of the process until it reaches a plateau at steady state with an average

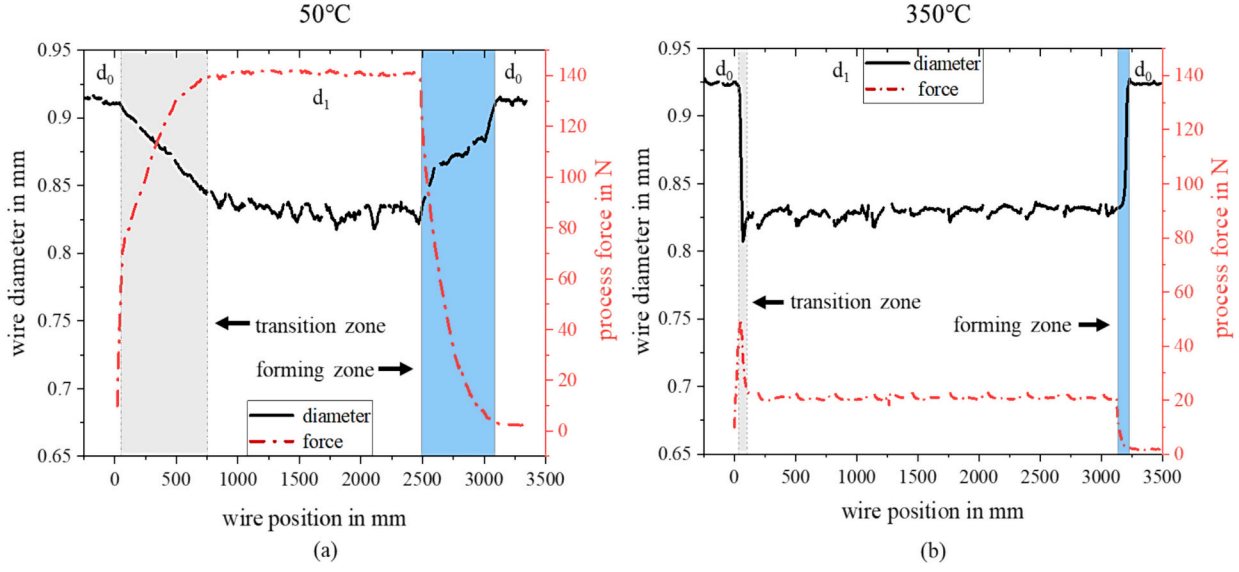

Fig. 2. Influence of the temperature on diameter and force evolution at 10 mm/s feeding speed and 20 % cross-sectional area reduction. (a) For experiment done at 50 °C with long forming zone (582 mm). (b) For experiment done at 350 °C with significantly shorter forming zone (82 mm).

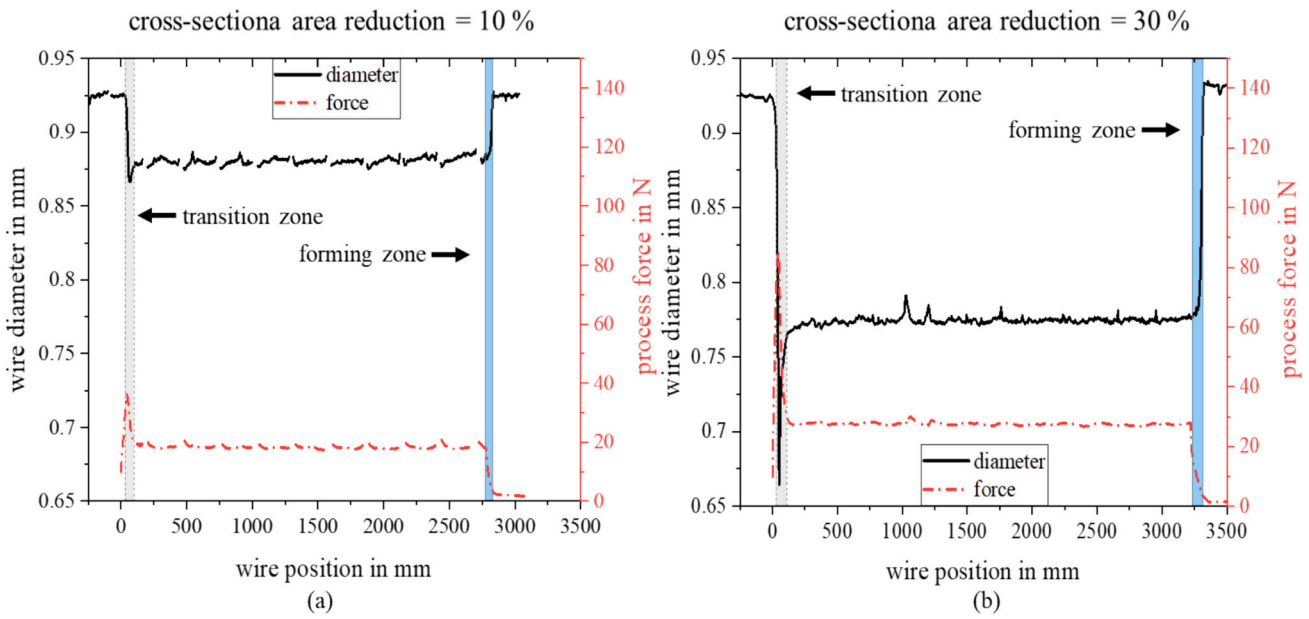

Fig. 3. Influence of the cross-sectional area reduction on diameter and force evolution at 350 °C and 10 mm/s feeding speed. (a) For experiments done with 10 % cross-sectional area reduction with short forming zone (50 mm). (b) For experiments done with 30 % cross-sectional area reduction resulting with slightly longer forming zone (64 mm).

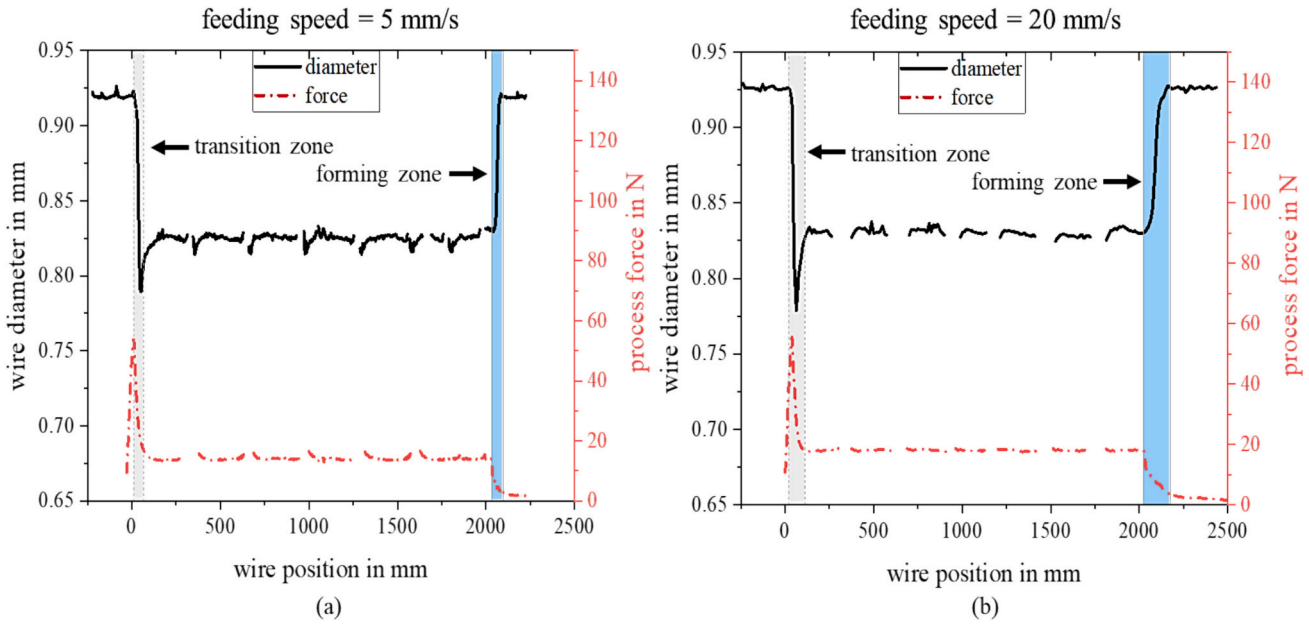

Fig. 4. Influence of the feeding speed on diameter and force evolution at 350 °C and 20 % cross-sectional area reduction. (a) For experiments done at 5 mm/s feeding speed with short forming zone (44 mm). (b) For experiments done at 20 mm/s feeding speed with slightly longer forming zone (137 mm).

force of 141 N. At the end of the experiment and thus for the measurement of the forming zone, the force drops back to zero as the drawing speed is set to the feeding speed. The drop in force takes the same time as the change in diameter from the final diameter back to the initial diameter. At 350 °C, the force also increases at the beginning of the process but results in a force overshoot as the force decreases due to the temperature induced softening of the material, until it stabilises at an average force of 21 N in the steady state. At the end of the experiment, the forces drop to zero in the same way as in the 50 °C experiment.

At higher temperatures, materials generally deform more easily because they have lower yield and flow stresses. In addition, dynamic recovery or recrystallisation can occur more readily, which helps to localise the deformation by softening in specific regions of the material [30], resulting in a shorter and more localised deformation. The accelerated recrystallisation and recovery processes can reduce work hardening [31], concentrating the deformation in a shorter region. Higher temperatures often increase strain rate sensitivity [32], i.e. the material flow stress increases more as the strain rate increases. Whilst higher temperatures reduce the yield stress at which a material begins to deform plastically, the total drawing force can increase if the deformation becomes highly localised. This localisation can lead to higher peak stresses in the material, particularly if work hardening occurs before significant thermal softening mechanisms can take place, as can be seen from the force overshoot at the start of the transition zone in Fig. 2 (b). In

earlier work in [23,26], the temperature induced length is analysed using FEM simulations and its influence on the forming zone length and the process window are investigated. The length of the heated zone was found to be consistent and not shorter than the forming zone for the areas relevant to the current experiments. While the temperature effect is directly included in our analysis in sections 3.4 and following, the heated zone is thus indirectly considered in the analytical approach presented.

3.2. Influence of the reduction ratio

Fig. 3 shows the diameter measurements in grey and the force measurements in red over the wire length for (a) 10 % CSA reduction ratio with $v_1 = 11.12$ mm/s and (b) 30 % CSA reduction ratio with $v_1 = 14.3$ mm/s. Both experiments are performed at 10 mm/s feeding speed and 350 °C. The transition zones are shown in light grey and the forming zones are shown in light blue.

The diameter and the force measurements in both reduction ratio plots appear similar when compared to the curves from the 350 °C experiment in Fig. 2 (b). Both plots show relatively short transition and forming zones in the diameter measurements and a force peak before the steady state, both indicative of localised deformation. Comparing Fig. 3 (a) and (b), differences can be seen despite the same curve schemes. When the drawing speed is increased from 11.12 to 14.3 mm/s (increase from $R = 10$ % to $R = 30$ %) with the feeding speed remaining the same, the final diameter continues to decrease in line with the volume constancy. In addition, there is a significantly greater undershoot that can be seen in the diameter curve and a significantly greater overshoot in the force curve with a higher CSA reduction at the beginning of the process. The length of the forming zone slightly increases from 50 mm (R = 10 %) to 64 mm (R = 30 %) and the average force in the steady state of the process increases from 18 N (R = 10 %) to 25 N (R = 30 %).

The CSA reduction directly affects the amount of deformation the material will undergo. A higher speed difference means a higher reduction ratio, thus a greater reduction in CSA and therefore more deformation. Therefore, a higher CSA reduction ratio means that more material must be plastically deformed in the same amount of time. The material must be deformed more, resulting the deformation being spread over a greater distance to avoid localised failure. This generally requires a longer forming zone to evenly distribute the increased deformation and provide a more gradual and uniform strain distribution. The process force required to draw the wire is directly related to the flow stress and the CSA reduction. Higher CSA reductions result in greater plastic deformation and therefore greater work hardening [10]. Particularly at the beginning of the process, when work hardening occurs before significant thermal softening of the material occurs, this results in a higher force overshoot at higher CSA reduction as it can be seen in both graphs. At higher CSA reduction ratios, the increasing work hardening increases the flow stress [33], resulting in higher drawing forces, and it increases the total strain, which can also result in higher flow stresses due to the strain rate dependent material response. This increased flow stress requires higher process forces to achieve the same feeding and drawing speeds assuming a constant volume.

3.3. Influence of the feeding speed

Fig. 4 shows the diameter measurements in grey and the force measurements in red over the wire length reconstructed from the process time for (a) 5 mm/s and (b) 10 mm/s feeding speed. Both experiments are performed at 350 °C and 20 % CSA reduction. The transition zones are marked in light grey and the forming zones in light blue again.

Again, both graphs show the same curves of localised deformation, although differences between (a) and (b) are also visible here. However, these differences are more pronounced as in Fig. 3. Both diameter curves result from the same CSA reduction, resulting in the same final diameter, but again the diameter measurements show a greater undershoot for the higher feeding speed and a larger overshoot for the force curve for the faster feeding speed. The forming zone extends from 44 mm ($v_0 = 5$ mm/s) to 137 mm ($v_0 = 20$ mm/s) and the average steady state force increases slightly from 16 N ($v_0 = 5$ mm/s) to 19 N ($v_0 = 20$ mm/s).

The strain rate is proportional to the feeding speed and strain rate sensitive materials (strain rate sensitivity exponent $n > 0$) show an increase in yield stress with increasing strain rate [34]. To accommodate higher strain rates without causing localised failure, the length of the forming zone tends to increase. This allows the material to deform more gradually, spreading the strain over a longer distance. Although the temperature and CSA reduction remain constant, the increased strain rate results in higher flow stresses and therefore a slight increase in process force. One reason for the greater influence of the feeding speed on the forming zone compared to the CSA reduction could be the indirect effect of the feeding speed on the temperature development in the wire. In order to achieve the same desired temperature at higher feeding speeds but at the same induction frequency, the generator power must be increased accordingly. This in turn may result in a different heating behaviour of the wire, which may not be as uniform or thorough as at lower feeding speeds. A possible uneven heat distribution at higher feeding speeds is also numerically recognised by Naughton et al. in [35]. Even if the temperature measurement during the experiment or induction simulations using the finite element method [23] indicate the desired wire temperature and through heating, the temperature-related behaviour of the material to the applied tensile stress may be different, resulting in less localised deformation. This could be a major limiting factor for the DD process as high drawing speeds are essential for industrial processes, especially mass production.

In general, the previous sections confirm that temperature has the greatest influence not only on the feasibility of the selected process parameters, but also on the localisation of the deformation and thus on the stability of the process. However, CSA reduction and feeding speed can also contribute to more or less localised deformation, so all three process parameters (T, v_0, v_1) and material properties must be taken into account when further analysing the forming zone.

3.4. Analysis of the forming zone

In plastic deformation, the flow criterion, flow stress and strain rate sensitivity are key factors in determining the behaviour of the material. Based on the previous section on the main influencing factors, the relationship between the strain rate, the feeding and drawing speeds v_0 and v_1 respectively, temperature and material properties must be considered to understand the effects on final diameters and forming zone lengths.

Assuming a constant strain rate in the forming zone and that the average drawing speed ½ ($v_0 + v_1$) acts in the forming zone, a simplified strain-based approach can be worked out. Using the effective strain ε (derived from the degree of deformation $\varphi = \ln(A_0/A_1)$ under the volume consistency assumption), the strain rate $\dot{\varepsilon}$ and the time t_{fz} the material spends in the forming zone, the length of the forming zone l_{fz} would be given by:

$$\dot{\varepsilon} = \frac{\varepsilon}{t_{fz}} = \frac{ln\,(v_1/v_0)}{t_{fz}} \left(with\ t_{fz} = \frac{2\,l_{fz}}{(v_0 + v_1)} \right), \tag{7}$$

$$l_{fz} = \frac{ln\,(v_1/v_0)(v_0 + v_1)}{2\,\dot{\varepsilon}}. \tag{8}$$

This equation is a geometric approach that does not take into account that the strain rate $\dot{\varepsilon}$ is typically a function of the flow stress and the temperature dependent behaviour of the material. To account for this strain rate and temperature sensitivity, the commonly used Zener-Holomon Eq. [36] is applied:

$$Z = \dot{\varepsilon}\, exp\left(\frac{Q}{RT}\right) \tag{9}$$

Z represents the Zener-Holomon parameter, Q the activation energy for plastic deformation of the material, R the universal gas constant and T represents the absolute temperature. This constitutive equation using Z can also be written as using a power law equation as follows:

$$Z = A_Z \sinh(\alpha\sigma_f)^n \tag{10}$$

Here, A_Z and α are material constants, σ_f represents the flow stress and n is the strain rate sensitivity exponent. Combining (9) and (10) leads to

$$\dot{\varepsilon} = A_Z \sinh(\alpha\sigma_f)^n \exp\left(-\frac{Q}{RT}\right) \tag{11}$$

The material constants A_Z, α and the strain rate sensitivity n can be determined by fitting flow stresses obtained from tensile tests at different temperatures and strain rates to the Zener-Holomon relation which has been described by Ryan and McQueen [37]. For the material used in this study, the material parameters are determined from the above-mentioned fitting of flow curve analysis (9) and (10) following Zhang et al. [38], who present the fitting procedure based on the empirical model from Ryan and McQueen [37] nicely. It is important to note that a good data base is essential for determining the parameters for the Zener-Holomon equations and thus for the analytical calculation of the forming zine length. During the parameter determination, it can be seen in Fig. 5 that the slope through the data points changes and increases with higher values of ln(sinh), which can be associated with the data from the 50 °C tensile test data. The underlying difference in material behaviour at this low temperature is reflected in the observation that localisation does not occur during DD processing, unlike at higher temperatures. In the following, the slope of the linear fit at the lower values of ln(sinh) corresponding to linearisation through the 150 and 250 °C data (red regression line) is used as the 50 °C DD experiments are not in the temperature range for localised forming zones. The ZX10 parameters obtained used for further calculations are: α = 0.0049, Q = 234 kJ/mol, A_Z = 3.006E+24 1/s and n = 23.3.

The flow stress σ_f (required for (11)) of a material is typically a function of the temperature. As the sinh-term of the equation is very sensitive to differences in the calculated flow stress, it is recommended that the term is carefully determined. To avoid error potentiation in the determination of the flow stress and its substitution in the susceptible sinh-term, a phenomenological determination based on the Zener-Holomon relations of the sinh-term is chosen by fitting the sinh-term vs. temperature data (see Fig. 6). The resulting regression relationship is then used as (12) to determine the sinh-term used for further

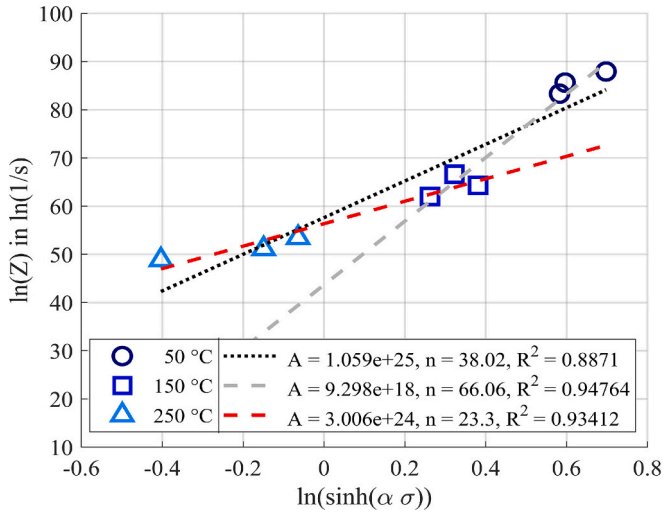

Fig. 5. Linearization of Zener plot data showing low and high temperature regions.

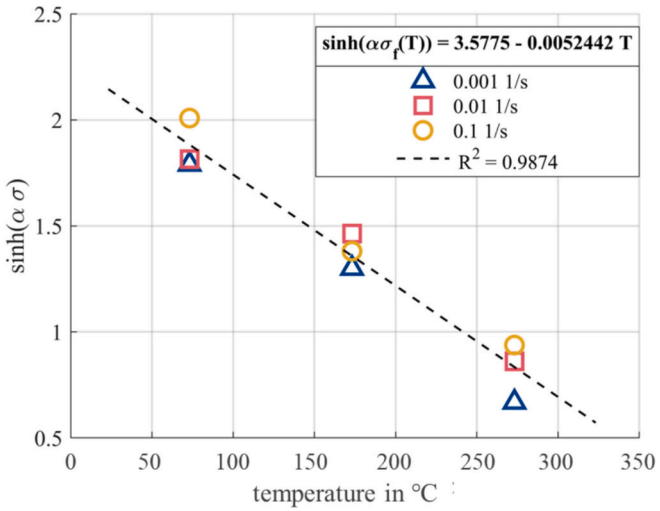

Fig. 6. *Linear regression fit for flow stress approximation for* (12).

calculations. In the case of large strain rate effects, it is recommended to determine the term according to strain rate ranges. For other data sets (such as different materials and concurrent different temperature or speed settings) than those shown in this study the respective slopes for the empirical approximation shown in Fig. 6 needs to be adjusted accordingly.

Using a regression approximation, the sinh-term for the ZX10 wires used in this study can be determined with the above obtained α by:

$$S(T) = \sinh(\alpha\sigma_f(T)) = 3.5775 - 0.0052442\,T \tag{12}$$

Substituting the term from (12) into the strain rate equation from (11), which can then be substituted into (8) to calculate the forming zone length l_{fz}, gives:

$$l_{fz}(T) = \frac{\ln\left(\frac{v_1}{v_0}\right)(v_0 + v_1)}{2\,A_Z\,S(T)^n \exp\left(-\frac{Q}{RT}\right)} \tag{13}$$

Fig. 7 shows the forming zone length versus temperature for the experimental DD data in open symbols and the analytical results from (13) in lines. The expected evolution from long forming zones to shorter ones with increasing process temperature is clearly visible. Variations in the experimental data can be seen, especially in the extreme cases for high CSA reductions and at higher feeding speeds. The analytical calculation of the deformation zone shows good agreement with the experimental values for temperatures above 150 °C. The non-localised deformation zones for lower temperatures below 150 °C deviate from the experimental data, which can be attributed to the adapted temperature range of the evaluated linearisation of the Zener plot data (see Fig. 5). These deviations occur because the Zener linearisation used to model the material deformation yields different results in different temperature ranges and the ranges in which there is no pronounced yielding behaviour of the material cannot be considered separately at this point. At lower temperatures, the selected Zener linearisation can lead to less accurate predictions of the length of the deformation zone because material properties such as ductility and strength are more strongly influenced by temperature. This leads to a discrepancy between the plot based on the analytical model and the actual experimental data. On the other hand, a variation of the forming zone length at the same temperature (influence of v_0 and v_1/v_0) can be represented. This shows that the length of the forming zone, which has a significant influence on a stable DD process and accurate CSA reductions, can be determined not only by FEM simulations but also on the basis of the process parameters of temperature, feeding and drawing speed and material parameters

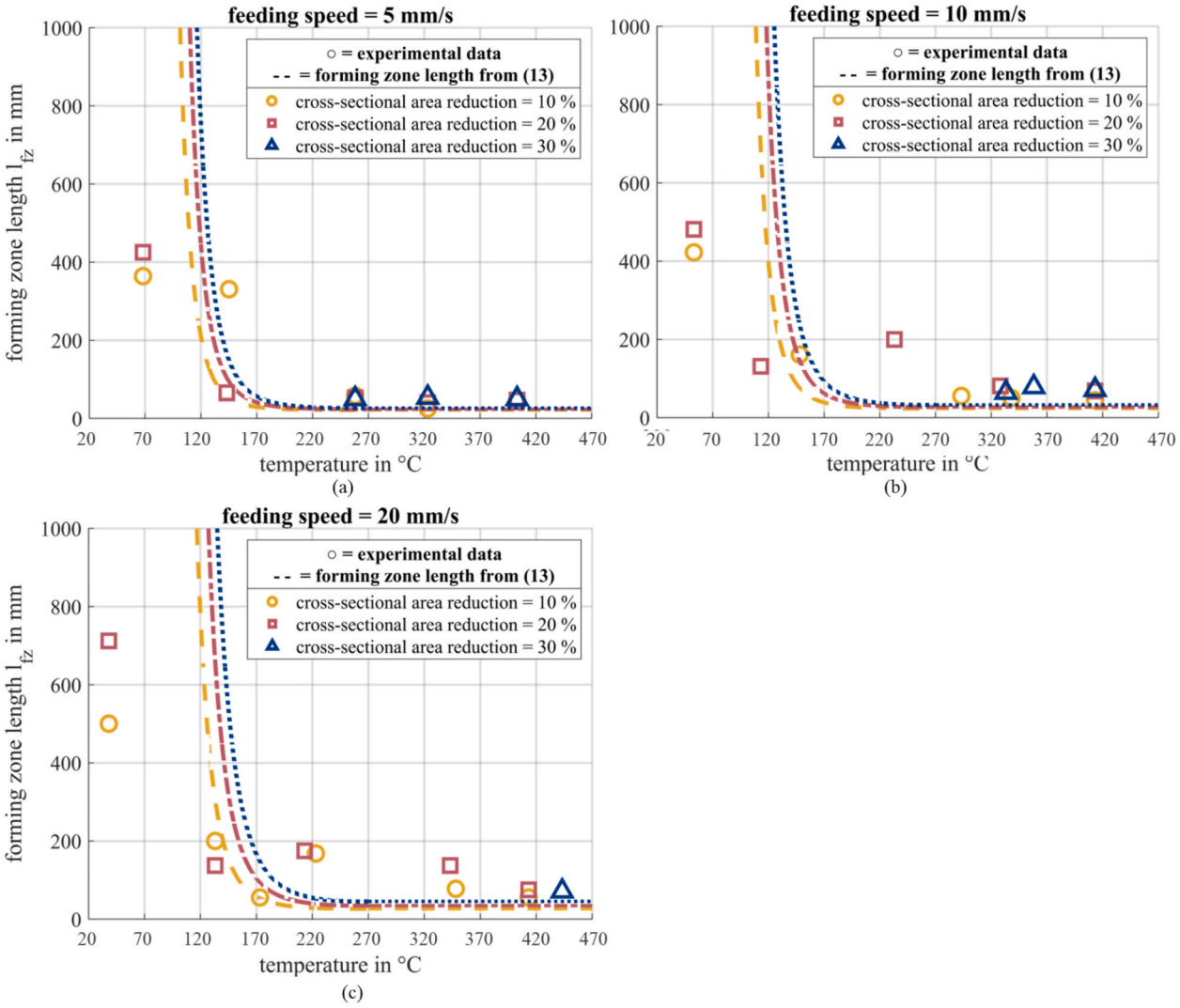

Fig. 7. ***Forming zone length*** **vs.** ***temperature for different cross-sectional area reductions comparing the analytical forming zone length from*** **(13)** ***with the experimental data.*** *(a) for feeding speed 5 mm/s, (b) for feeding speed 10 mm/s and (c) for feeding speed 20 mm/s, showing good agreement for higher temperatures.*

(from a set of flow curves). The established equation can also be applied to other metals in the DD process due to the material specific considerations.

3.5. Stable process condition

Not only the experimental data, but also the regression and the analytical calculation of l_{fz} indicate that there must be a minimum length of l_{fz} that is greater than zero for stable process settings. The smaller the l_{fz} value, the better the process settings achieve an ideal deformation case. Assuming that the free wire length l_{free} between the wire spools can be separated into the areas of cold wire and the area of heated wire (see Fig. 1), the temperature increase from the cold to the heated wire must be significant in order to localise the deformation. In simple terms, this means that the stiffness of the wire in the cold wire area must be significantly greater than the stiffness of the wire in the heated wire area and therefore the deformed area (l_{fz}). The respective stiffnesses of the wire parts mentioned can be used to put this relation into perspective: The axial elastic stiffness C of a rod can be calculated from $C = EA/L$, using the Young's modulus E of the material and the dimensions CSA A and length L of the rod. The minimum stiffness of the material at room temperature can be assumed using the smaller final CSA wire dimensions (A_1). In the deformation zone, the Young's modulus is not suitable for describing the plastic axial stiffness. Here, the tangent modulus $E_t = d\sigma/d\varepsilon$, which can be determined above the proportional limit (plastic region) in strain-stress curves, describes the material behaviour. The maximal stiffness for the heated wire area will be reached at the point of maximum CSA (A_0) at the beginning of the forming zone and the corresponding temperature dependent tangent modulus. A condition for a stable process, using the required approximation of the minimum forming zone length l_{fz}, would therefore be as follows:

$$C_{l_{fz}} \ll C_{l_{free}} \tag{14}$$

$$\Leftrightarrow E_t(T)\,\frac{A_0}{l_{fz}} \ll E\,\frac{A_0 \frac{v_0}{v_1}}{(l_{free} - l_{fz})} \tag{15}$$

$$\Rightarrow l_{fz,min}(T) \gg \frac{E_t(T)\, l_{free}}{E\,\frac{v_0}{v_1} + E_t(T)} \tag{16}$$

The tangent modulus E_t can be a function not only of temperature, but also of strain rate. This must be taken into account depending on the material used. The tangent modulus can be determined from stress-strain curves or by using the Ramberg-Osgood relation [39,40]:

$$E_t = \frac{E\,\sigma_{TYS}}{\sigma_{TYS} + 0.002\,RO\,E\left(\frac{\sigma}{\sigma_{TYS}}\right)^{RO-1}}, \tag{17}$$

with the yield stress σ_{TYS} and the Ramberg-Osgood parameter RO using the fracture strain ε_{max} and the ultimate tensile strength σ_{UTS}:

$$RO = \frac{ln\left(\frac{\varepsilon_{max} - \sigma_{UTS}/E}{0.002}\right)}{ln\left(\sigma_{UTS}/\sigma_{TYS}\right)} \tag{18}$$

For the ZX10 wires used, the tangent modulus is determined from the stress-strain curves at various temperatures and strain rates as the tangent $E_t = d\sigma/d\varepsilon$ at the start of the plastic region. The temperature dependent function of $E_t(T)$ is then determined by regression through the plotted E_t values over the respective temperature.

Using parameters of the experimental setup, the Young's modulus E = 44.7 MPa of pure magnesium and fixing the feeding speed to v_0 = 10 mm/s, the minimum forming zone length can be calculated from (16) as a function of temperature and drawing speed as shown in Fig. 8. Depending on the used drawing speed v_1, where higher v_1 at a constant v_0 mean higher CSA reductions, different minimum forming zone lengths result depending on the process temperature. Again, a localisation of the forming zone with increasing temperature can be observed. The longer forming zone required for higher CSA reduction, which was discussed in the previous section, is also visible. In addition, the minimum forming zone length does not drop to zero at higher temperatures. This provides an analysis of how process variables affect process stability and offers a process and material parameter based approach to process control. On the basis of (16), e.g. the process parameter pair v_0 and v_1 can be optimised and maximised by minimising $l_{fz,min}$, thus ensuring a stable DD process in the steady state by means of localised deformation.

However, since the determination of the minimum forming zone length, which can be easily localised by means of a temperature rise, cannot be instinctively introduced into the process, the following section is devoted to the estimation of a maximum drawing speed v_1 at a fixed feeding speed v_0, resulting in a maximum CSA reduction in a single drawing pass. The maximum stable CSA reduction is limited by the ability of the material to undergo plastic deformation without failure. Particularly at high temperatures, the tensile drawing stress from the speed difference and the flow stress of the material tend to be low, allowing only small variations in these values without failure. In order to ensure that the material will still be able to withstand the deformation and not fracture during experiments, the possible plastic deformation work is considered. The plastic deformation work W_p in the forming zone l_{fz} from the strain at the beginning of the deformation $\varepsilon_{initial}$ to the strain at the end of the deformation ε_{final} can be written as:

$$W_p = A_0\,l_{fz}\int_{\varepsilon_{initial}}^{\varepsilon_{final}} \sigma(\varepsilon)\,d\varepsilon \;with\; \varepsilon_{final} = ln\left(\frac{A_0}{A_1}\right) = ln\left(\frac{v_1}{v_0}\right) \tag{19}$$

Simplifying the equation assuming constant strain rate in the forming zone, considering temperature dependency and using the minimum forming zone length $l_{fz,min}$ from (15), gives:

$$W_p(T) = A_0\,l_{fz,min}\,\sigma_f(T)\,ln\left(\frac{v_1}{v_0}\right) \tag{20}$$

As an upper limit, the maximum possible work that the material can withstand can be determined by evaluating the area under the representative stress-strain curves. For a temperature dependent function of this maximum theoretical work, the calculated values can be plotted against the corresponding temperatures and determined by regression through the data points. All drawing speeds v_1, set in (20), which remain below this maximum work value can be considered to be physically feasible.

Fig. 9 shows the plastic work in the deformation zone from (20) vs. the temperature with coloured lines for different drawing speeds v_1 and the maximum possible theoretical work (determined from representative stress-strain curves as regression function over temperature) as black line. The grey coloured area above the maximum plastic work line marks the unstable process parameter settings for the selected parameters, as the material, because the plastic work W_p required to achieve these drawing speeds v_1 at a constant feeding speed is exceeded by the maximum theoretically absorbable plastic work of the material used. In this way, the maximum possible CSA reduction can be predicted for different process parameter settings. Using this approach, at a forming temperature of 325 °C and a feeding speed of 10 mm/s, the theoretical maximum CSA reduction would be at a v_1 of 15 mm/s, corresponding to a CSA reduction of 33.33 %, while the theoretical maximum at a forming temperature of 425 °C would be a CSA reduction of 44.44 %.

4. Improvement of diameter reduction prediction

The equations used in DD are based on the assumption of ideal plastic deformation. Nevertheless, there are differences between the analytically calculated (R_{an}) and the measured (R_{exp}) CSA reductions and not

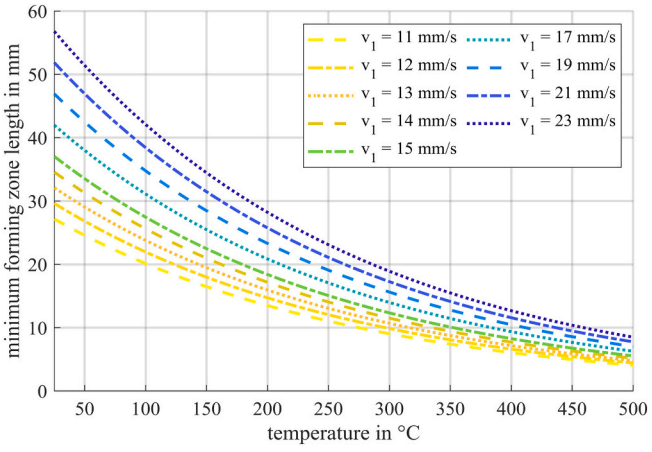

Fig. 8. *Minimum forming zone length from (16) vs. temperature for 10 mm/s feeding speed and different drawing speeds v_1, showing longer minimum forming zone lengths at higher drawing speeds and lower temperatures.*

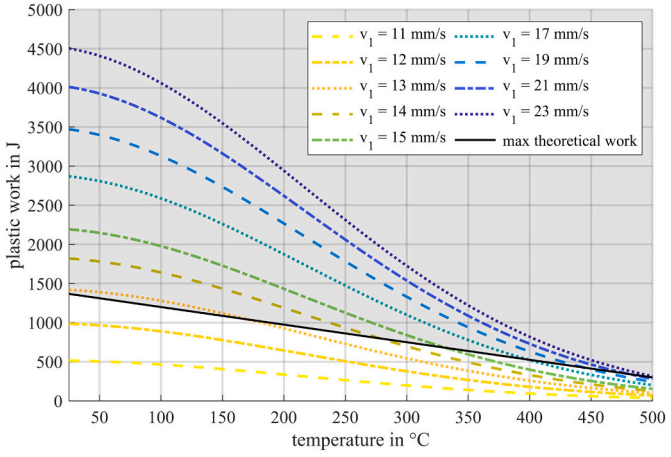

Fig. 9. *Plastic work from (16) vs. temperature for 10 mm/s feeding speed and different drawing speeds v_1. It shows less plastic work required as the drawing speed decreases and the temperature increases. The drawing speed lines within the grey area above the maximum theoretical work (dashed line) represent infeasible process parameter settings.*

all process parameter settings can result in localised deformation as shown above. A difference between the two reduction values (see (3) and (4)) violates the established steady state condition of the process. However, since the volume constancy applies to the DD process in all cases, there must be other factors in addition to the assumption of ideal plastic deformation that could cause these deviations. In general, deviations can be caused by:

- *Measurement inaccuracies* such as experimental measurement or instrument calibration errors.
- *Material variations* such as in material properties or inhomogeneous initial diameter over the length of the wire, resulting in inhomogeneous deformation. Or volume redistribution where the wire may experience axial elongation or bulging due to complex stress and strain distributions during the drawing process.
- *Temperature variations* caused by temperature gradients, temperature inhomogeneity, or variations in heating efficiency e.g. due to differences electromagnetic field distribution of the induction coil or changes in wire diameter.
- *Dynamic effects* such as strain rate sensitivity of the (inhomogeneous) material, which can lead to different deformation behaviour during the process. Or vibrations, oscillations or speed changes in the drawing setup, which can cause variations in the deformation process.

However, deviations due to e.g. measurement inaccuracies or inhomogeneous material properties can be categorised as systematic errors and not as process-related deviations and therefore cannot be used to explain the differences between R_{an} and R_{exp} values. To account for temperature variations and dynamic effects that are process or setup related (the process non-idealities), we propose to use the correction factor η. Using (2)–(4), which considers for the ideal deformation case, the predicted CSA reduction R_{pred} corrected by η can then be expressed as:

$$R_{pred} = 1 - \frac{\eta\, A_{1,ideal}}{A_0} = 1 - \eta \frac{v_0}{v_1} \tag{21}$$

In the following sections the correction factor η is be determined in three ways: *First,* by defining a theoretical correction factor using an energy balance equation; *second,* by proposing an empirical model calculation for an existing experimental data set; and *third,* by proposing a simplified process accuracy estimation equation.

4.1. Energy balance equation

The first law of thermodynamics is a formulation of the energy conversation and is often expressed as the sum of the contributions from the work done on or by the system and the amount of heat added to or removed from the system.

The components of the energy balance equation for the DD process are then:

1. Thermal energy term introduced into the system by induction heating: Q_{ind}.
2. The mechanical work done by the forces in the process: W_{mech}.
3. The convective heat loss due to cooling on air: Q_{conv}
4. The energy dissipation Q_{diss} due to thermal radiation and non-idealities in the process by the correction factor η.
5. The elastic deformation energy: Q_{elas}.
6. The thermal energy stored in the material: Q_{stored}.

In the DD process, the thermal energy Q_{ind} is due to the temperature applied to the system by the induction heating power P_{ind} over the length of the induction coil l_{coil} and during the time *t* it takes the wire to pass through the coil:

$$Q_{ind} = P_{ind}\, t = P_{ind}\, \frac{l_{coil}}{v_0} \tag{22}$$

It is assumed that the heating power P_{ind} is constantly applied onto the wire and that the wire passes through the coil at the feeding speed v_0 since the deformation of the wire starts at the point of maximum temperature, which is reached directly at the end of the induction coil. In addition, P_{ind} represents the energy transmitted to the wire and therefore depends on the setup configurations used, with the power supplied by the induction generator and its loss depending on the number of windings of the induction coil and the mass, material and emission factor of the wire passing through.

The mechanical work W_{mech} done by the drawing force (with stress in tensile direction σ and wire CSA A) in the process is assumed to be constant when the steady state is reached:

$$W_{mech} = \int_0^{l_{fz}} \sigma\, A\, dx = \sigma\, A\, l_{fz} \tag{23}$$

Since (23) describes the effective stress of the completed deformation process and thus the total applied deformation energy applied and the force is constant in the steady state, the continuous change of CSA over the forming zone length is taken into account.

Based on Newton's law of cooling, the convective heat energy loss Q_{conv} during the cooling time is calculated from the convective heat transfer coefficient *h*, the wire surface area A_s and the ambient temperature T_{amb}. The segment of the wire that experiences significant convective heat loss is the heated wire region after leaving the induction coil, i.e. the time the wire takes to pass through the forming zone t_{fz} (see (7)). Thus, Q_{conv} can then be calculated as:

$$Q_{conv} = \int_0^t h\, A_s\, (T - T_{amb}) = h\, A_s\, (T - T_{amb}) \frac{2\, l_{fz}}{(v_0 + v_1)} \tag{24}$$

The dissipation energy lost due to thermal radiation and process non-idealities Q_{diss} is expressed using the correction factor η:

$$Q_{diss} = \eta\, (Q_{ind} + W_{mech}) \tag{25}$$

The energy balance equation should take into account the length of wire undergoing elastic deformation. In a continuous dieless wire drawing process, this typically includes the part of the wire between the two spools that has not yet been plastically deformed. Therefore, the free wire length between the two spools, which is not heated and remains in the elastic region, should be considered as this length represents the part of the wire that can store elastic energy. To describe the elastic energy term Q_{elas}, the Young's modulus *E* of the material and the free unheated wire length volume V_{free} between the two wire spools are used:

$$Q_{elas} = \frac{1}{2}\, E\, \varepsilon^2\, V_{free} \tag{26}$$

The stored thermal energy Q_{stored} is a function of temperature over the wire length using the wire's mass *m* and the specific heat capacity c_p of the material:

$$Q_{stored} = m\, c_p\, (T - T_{amb}) \tag{27}$$

The sum of the components from (22) through (27) expresses then the energy balance equation for the DD process and can be rearranged to calculate the correction factor η:

$$Q_{ind} + W_{mech} = Q_{diss} + Q_{conv} + Q_{elas} + Q_{stored}\,, \tag{28}$$

$$\begin{aligned} \Rightarrow P_{ind}\, \frac{l_{coil}}{v_0} + \sigma\, A\, l_{fz} = \eta \left(P_{ind}\, \frac{l_{coil}}{v_0} + \sigma\, A\, l_{fz} \right) \\ + h\, A_s\, (T - T_{amb}) \frac{2\, l_{fz}}{(v_0 + v_1)} + \frac{1}{2}\, E\, \varepsilon^2\, V_{free} \\ + m\, c_p\, (T - T_{amb}) \end{aligned} \tag{29}$$

$$\Rightarrow \eta = 1 - \frac{h\,A_s\,(T - T_{amb})\,\frac{2\,l_{fz}}{(v_0+v_1)} + \frac{1}{2}\,E\,\varepsilon^2\,V_{free} + m\,c_p\,(T - T_{amb})}{P_{ind}\,\frac{l_{coil}}{v_0} + \sigma\,A\,l_{fz}}. \quad (30)$$

To calculate the theoretical correction factor η from (30), the previously determined Zener parameters and the flow stress $\sigma_f(T)$ from the regression approximation for the sinh-term are used. The process setup parameters are fixed using a feeding speed of $v_0 = 10$ mm/s, the initial CSA A_0, the induction coil length $l_{coil} = 20$ mm and the free wire length $l_{free} = 745$ mm between the two wire spools of the setup. The Young's modulus $E = 44.7$ MPa, the density ρ and the specific heat capacity c_p are taken from pure magnesium [41,42], treating ZX10 as a low alloy magnesium alloy. From these literature values, the temperature dependent parameters ρ and c_p are determined by regression fits to the literature data points (see Fig. 10 (a) and (b); literature data as open circles and regression as dashed line). The heat transfer coefficient range $h = 10$–100 W/m^{2}K for forced convection in air and the induction power P_{ind}, determined from induction heating experiments for FEM simulations in earlier work in [23], are used as fitting parameters.

Fig. 11 shows the theoretical correction factor η from (30) (lines) and the experimental data (open symbols; calculated from $\eta = R_{exp}/R_{an}$) as a function of the temperature for different feeding speeds. It is shown that the calculation of the theoretical correction factor as a function of the process temperature describes an approximation of the analytical to the experimental CSA reduction, with an increase in the correction factor η temperature ($\eta \to 1$) with increasing temperature. Although quite some assumptions and simplifications had to be made to calculate the theoretical correction factor η, the plot shows a good agreement between the experimental data points and the theoretical correction factor η. However, using the energy balance approach to calculate the correction factor η is a very complex approach, as it requires assumptions and simplifications or a detailed determination of the material properties or FEM analysis methods for the calculation. Alternatively, the correction factor η can also be determined and estimated using an existing experimental data set, or it can be estimated using process parameters and material properties as will be shown in the following sections.

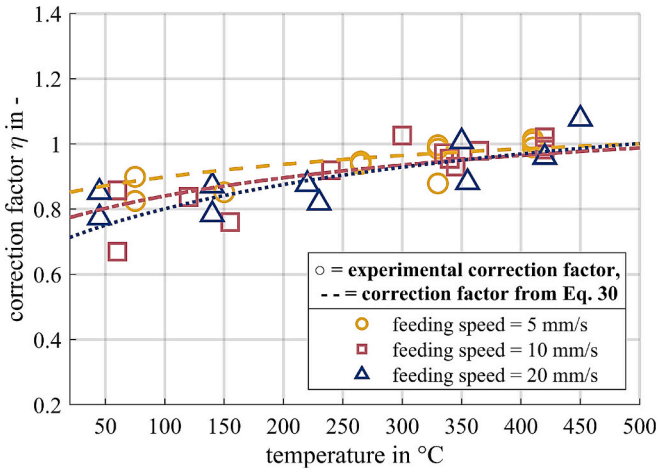

Fig. 11. *Correction factor* vs. *temperature for experimental data and from energy balance eq.* (30) *for different feeding speeds, showing good agreement of the two data sets.*

4.2. Empirical model calculation

A more practical approach to estimating the correction factor η is to use an already existing experimental data set for a multidimensional regression to obtain an empirical model. Obtaining the correction factor η with the empirical model calculation is therefore material and system specific, as it also takes into account non-idealities due to the chosen experimental setup.

Given *j* experimental data sets, where each set *i* provides values for the temperature, the feeding and drawing speed, the forming zone length and experimental CSA reduction, the correction factor η can then be calculated by fitting the empirical model using e.g. least square regression.

For the empirical model, the regression must be based on factors on which the correction factor depends on. As mentioned above, the accuracy of the CSA reduction achieved in the DD process is mainly influenced by the temperature, but also by the feeding and drawing speeds used. As the speeds directly influence the strain rate, the correction factor η can be a function of temperature and strain rate, or for a more practical approach by using the directly controllable process parameters as function of temperature, v_0 and v_1, e.g.:

$$\eta = f\,(\dot{\varepsilon}, T)\ with\ \eta_i = k_1\,T_i^2 + k_2\,T_i\,\dot{\varepsilon}_i + k_3\,\dot{\varepsilon}_i + k_4, \quad (31)$$

or a more practical approach with

$$\eta = f\,(v_0, v_1, T)\ with\ \eta_i = k_1\,T_i^2 + k_2\,T_i + k_3\,v_{0,i} + k_4\,\frac{v_{0,i}}{v_{1,i}} \quad (32)$$

For determining the coefficients $k_{1\ldots4}$, a least square regression formulation can be used:

$$with\ \eta_{exp,i} = \frac{R_{exp,i}}{R_{an,i}} \quad (33)$$

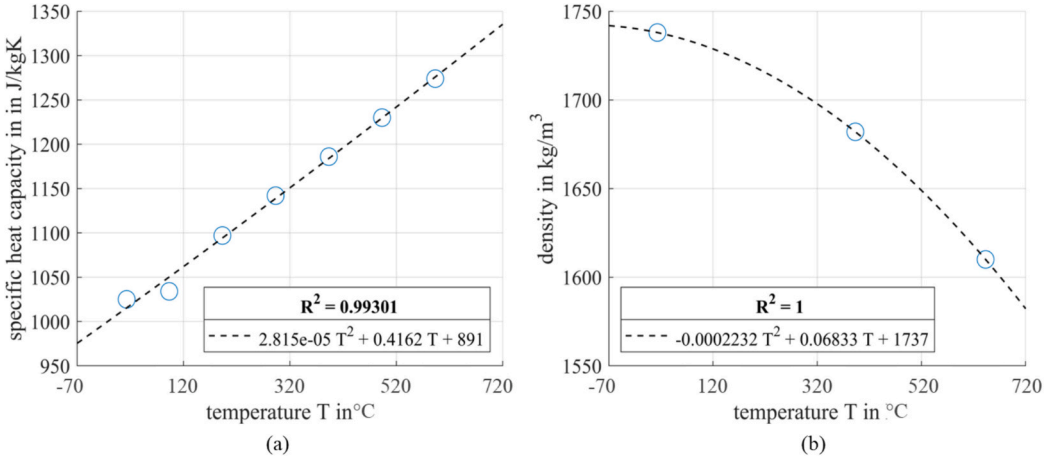

Fig. 10. Regression fit for temperature dependent material properties of pure magnesium. (a) Linear fit for heat capacity vs. temperature. (b) Quadratic fit for density vs. temperature.

$$\min_{k_{1\ldots4}} \sum_{i=1}^{j} \left(\eta_{exp,i} - \left(k_1 T_i^2 + k_2 T_i + k_3 v_{0,i} + k_3 \frac{v_{0,i}}{v_{1,i}} \right) \right)^2. \quad (34)$$

For the ZX10 data set used in this work, the coefficients determined from (34) are: $k_1 = -0.000001\ °C^{-2}$, $k_2 = 0.001232\ °C^{-1}$, $k_3 = -0.000825$ s/mm and $k_4 = 0.809962$. Substituting the determined coefficients $k_{1\ldots4}$, into (32), it is possible to predict the correction factor η for other process parameter settings for the same material, as can be seen in Fig. 12. The calculated correction factor over the temperature for different feeding speeds and CSA reductions is within the experimental data set and shows similar tendencies of η values closer to 1 at higher temperatures as shown for the energy balance equation above. Although the general tendency of the empirical model agrees with the experimental data in all subfigures, the plots show a limitation of the empirical model. Not all of the dashed curves show a good fit through the corresponding data points and the differences between the CSA reductions in the plots of the individual feeding speeds are not as distinct as they should be. The empirical model presented is suitable for a rough estimation of the correction factor and for incorporating the system-specific process non-idealities of the experimental setup. However, for a more precise estimation, a sufficiently large amount of data should be considered for the underlying least squares regression.

4.3. Simplified approximation based on the localization of deformation

The correction factor η essentially describes how close the chosen parameter settings of the DD process are to the ideal deformation case. Thus, the correction factor η is a factor describing the localisation of the process deformation, which is directly related to the length of the forming zone.

As mentioned above, the temperature is the main factor influencing the DD process. In Fig. 13, this influence can be seen on the diameter (a) and the force (b) evolution for temperatures from 50 to 420 °C for experiments carried out at the same feeding speed and same set CSA reduction. The diameter curves show that both the transition zone in the beginning and the forming zone measurements in the steady state are obviously temperature dependent. At lower temperatures of 50–250 °C, the diameter changes in the transition and in the forming zone are slower, which is reflected in a lower slope and more time required to establish the final diameter. The higher the temperature, the shorter

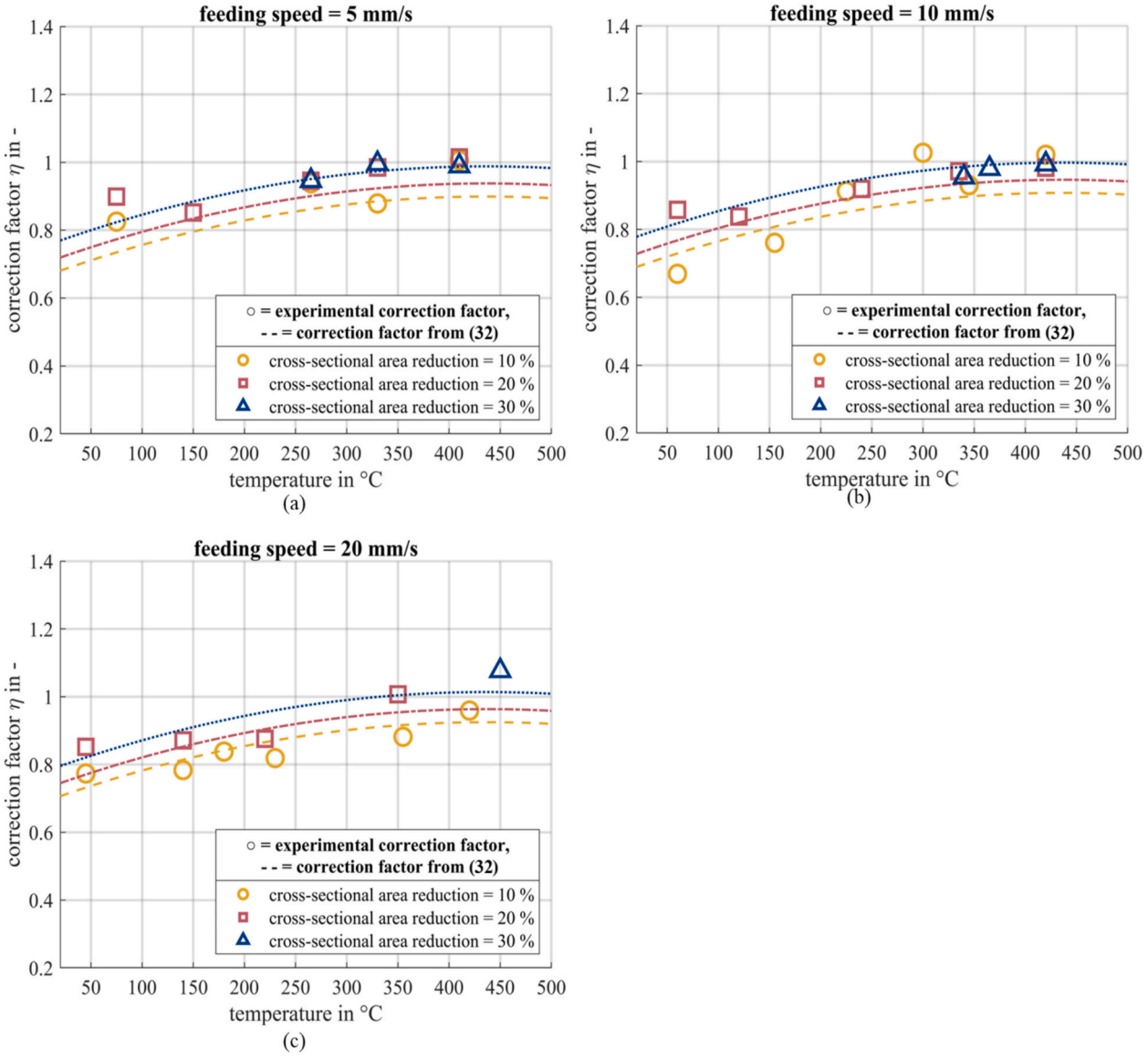

Fig. 12. ***Correction factor vs. temperature for experimental data and from empirical model calculation (32) for different cross-sectional area reductions.*** *(a) For feeding speed 5 mm/s, (b) for feeding speed 10 mm/s and (c) for feeding speed 20 mm/s, showing less good representation of the effects of feeding and drawing speed.*

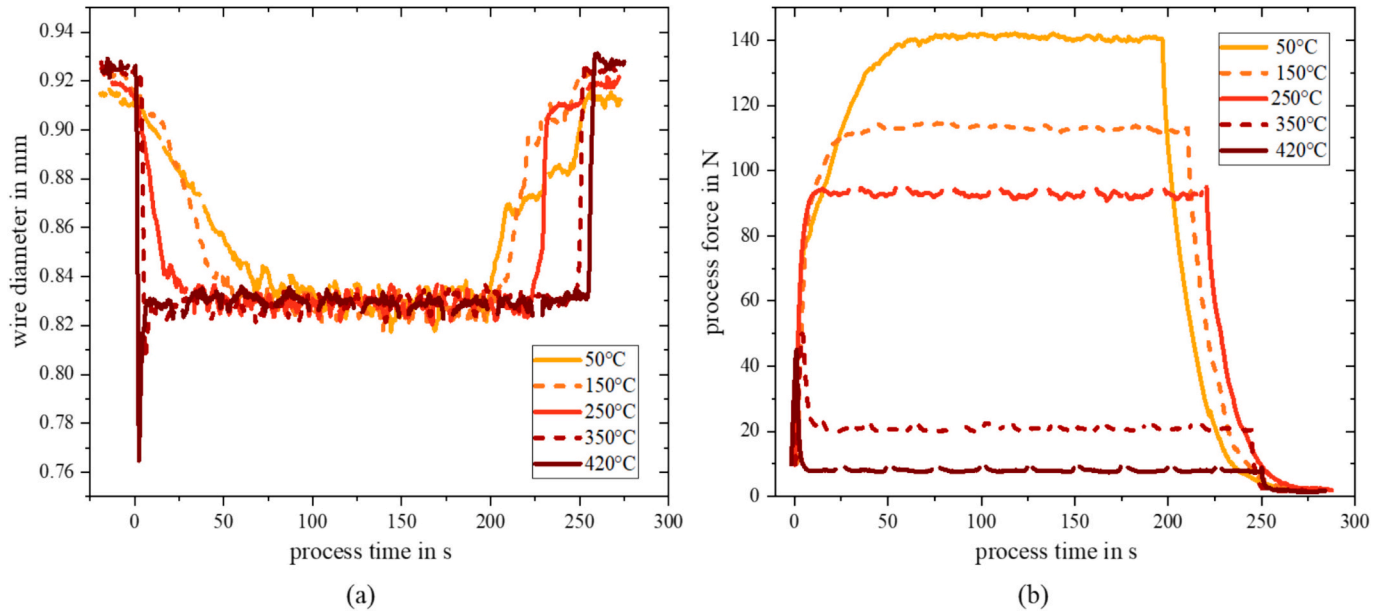

Fig. 13. Wire diameter and process force vs. process time done at 10 mm/s feeding speed and for 20 % cross-sectional area reduction. (a) Influence of the temperature on diameter evolution. (b) Influence of the temperature on force measurements. Both graphs showing localised deformation behaviour at elevated process temperatures.

both the transition and the forming zone become, and the more abrupt the diameter change, resulting in localised deformation. It is easy to see that an ideal deformation case with almost instantaneous diameter changes occurs in the diameter curves at 350 and 420 °C. Here, the measured final CSA reductions and the analytical CSA reductions are similar ($R_{exp} \approx R_{an}$) and the correction factor is $\eta \approx 1$. Fig. 13 (b) also shows the effect of temperature on the force measurements. The curves of the lower temperatures (50–250 °C) show the typical force curves of a non-localised deformation (see Fig. 2). In experiments with a lower feeding speed of 5 mm/s, the 250 °C measurement curves show localised behaviour. Therefore, there seems to be a turning point in the material behaviour at 250 °C where the feeding speed and thus the heating rates seem to play a role. At higher temperatures above 350 °C, the force curves again show the typical localised deformation of the ideal deformation case, with a force peak followed by a relatively low average force in the steady state. In our case, the ideal deformation case was achieved at high temperatures from 350 °C and upwards.

In summary, at high temperatures and with a small forming zone, the deformation of the wire is well localised, resulting in a correction factor of $\eta \approx 1$. As shown in the case of ZX10 above, the length of the forming zone depends primarily on the temperature of the wire. To further simplify the determination of η, the effects of the feeding speed and the speed ratio are neglected. Hot forming processes involve deformation and concurrent recrystallization at high temperatures, usually in the range of 0.6–0.8 times the melting temperature T_m of the material being formed. The experimental data and the theoretical correction factor in Fig. 11 suggest using a saturation curve model, or more simplified a 2nd order polynomial. To fit this polynomial for a simplified approximation of η, the vertex form of the parabola is used. This parabola reaches $\eta = 1$ at approximately 0.8 T_m, which is commonly used as the upper limit for hot working temperatures; and temperatures of 450 °C and above were not feasible in the ZX10 DD experiments. In addition, the parabola is compressed according to the temperature behaviour of the material. Therefore, an approximation of the correction factor η based on the localisation of the deformation can be as follows:

$$\eta(T) = \frac{-\sigma_{TYS}}{\sigma_f(0.6\ T_m)} \left(\frac{0.8\ T_m - T}{T_{amb}}\right)^2 + 1. \tag{35}$$

Here T, T_m and T_{amb} are the process temperature, the melting temperature of the material and the ambient temperature, respectively. The TYS of the material at ambient temperature σ_{TYS} and the ambient temperature T_{amb} are used to normalize the function to ensure a dimensionless correction factor η. The material's flow stress σ_f at a temperature of 0.6 T_m, which represents the starting temperature of good deformation localisation, is chosen as a phenomenological fit factor. This approach does not take into account very strain rate sensitive materials, large CSA reductions and system-specific process non-idealities like temperature variations (e.g. due to the heating or initial diameter fluctuations) or dynamic effects (e.g. vibrations, oscillations, or speed changes) in the drawing setup that can introduce variations in the deformation process.

Fig. 14 shows the correction factor η based on the experimental data (open symbols; calculated from $\eta = R_{exp}/R_{an}$) and the approximation from (35) (dashed line). Again, the calculated correction factor η as a function of temperature is within the experimental data set, although the effect of the base speed and the CSA reduction was not considered in this approach. Even though the approximation calculation does not reproduce the scatter of values to the same extent as the experimental

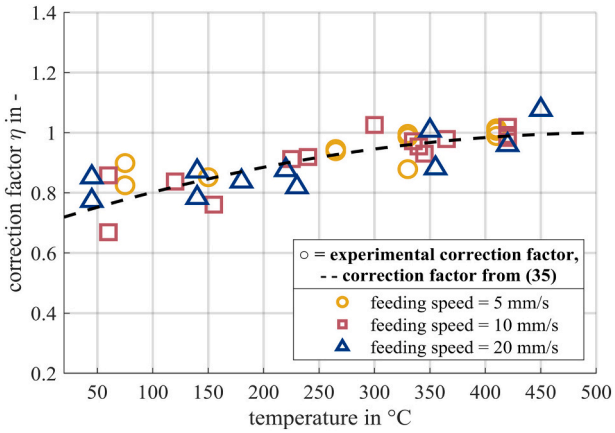

Fig. 14. *Correction factor vs. temperature for experimental data and from simplified approximation (35) for different feeding speeds, showing possible approximation to the experimental data.*

data, it still shows very good agreement with the η calculated from the experimental data. This shows that even in this case the correction factor η can also be predicted in a very simplified way, enabling a simple and process-control based adjustment of the DD process.

5. Conclusion

This paper analyses the influences on the forming zone in dieless wire drawing and improves the prediction of diameter reduction by introducing analytical equations for both. The main results are as follows:

- The forming zone length is determined by analysing the interaction between the process parameters temperature and speeds and the temperature dependent material properties. This involves an analytical equation for the forming zone length that describes the material flow and deformation in the dieless wire drawing process. The equation developed can be applied to other metals because of material-specific considerations.
- When the temperature exceeds 0.6 times the melting temperature of the material, the deformation becomes highly localised. This means the material deforms in a smaller region, leading to more precise control over the shape and size of the formed wire. The diameter and force curves in this scenario closely match an ideal deformation profile, indicating efficient and controlled forming.
- For the process to be stable, two key conditions must be met: The forming zone should be minimised to ensure localised deformation. And the maximum diameter reduction should be achieved without compromising stability. Equations for both conditions are presented in this paper.
- Elevated temperatures help in localising and stabilising the deformation process. However, increasing the feeding speed or the degree of diameter reduction can destabilise the process. This is because higher speeds and larger reductions require longer forming zones, which can lead to uneven deformation and potential defects. This presents a challenge for industrial applications where high speeds and significant reductions are often necessary for efficiency and productivity.
- In practical applications, the dieless wire drawing process may not always follow ideal conditions. A correction factor is introduced and determined to account for these process non-idealities. This factor helps to predict the actual diameter reduction and to understand how the deformation will be localised under real-world conditions. By incorporating this correction factor, the process can be better controlled and optimised.

CRediT authorship contribution statement

Merle Braatz: Writing – review & editing, Writing – original draft, Visualization, Validation, Methodology, Investigation, Formal analysis, Data curation, Conceptualization. **Jan Bohlen:** Writing – review & editing, Supervision, Conceptualization. **Noomane Ben Khalifa:** Writing – review & editing, Supervision, Conceptualization.

Statements and declarations

The authors declare that they have no conflict of interest.

This research did not receive any specific grant from funding agencies in the public, commercial or non-profit sectors other than the general funding of the Helmholtz Zentrum Hereon.

Declaration of competing interest

The authors declare that they have no known competing financial interests or personal relationships that could have appeared to influence the work reported in this paper.

Acknowledgements

The authors would like to thank Dr. Maria Nienaber for her help with the extrusion of the wires.

References

[1] Weiss V, Kot RA. Die-less wire drawing with transformation plasticity. Wire Journal 1969;2(9):182–9.
[2] Ohno A, et al. New tapered-rod forming process for Coil Springs. SAE Trans 1982: 471–8.
[3] Fann KJ, Hsu HY. Dieless drawing wire with a given end geometry by realizing temperature distribution evolution. J Phys Conf Ser 2022;2345(1). https://doi.org/10.1088/1742-6596/2345/1/012016.
[4] Wengenroth W, Pawelski O, Rasp W. Theoretical and experimental investigations into dieless drawing. Steel Research 2001;72(10):402–5. https://doi.org/10.1002/srin.200100141.
[5] Pawelski, O., W. Rasp, and K. Schmeisser. Dieless Drawing - A Forming Process Allowing Flexible Shape Generation. in Proceedings of the Thirty-First International Matador Conference. Palgrave. London: Springer; 1995. https://doi.org/10.1007/978-1-349-13796-1_61.
[6] Furushima T, Shirasaki A, Manabe K. Fabrication of noncircular multicore microtubes by superplastic dieless drawing process. J Mater Process Technol 2014; 214(1):29–35. https://doi.org/10.1016/j.jmatprotec.2013.07.005.
[7] Furushima T, Manabe K. Large reduction die-less mandrel drawing of magnesium alloy micro-tubes. Cirp Annals-Manufacturing Technology 2018;67(1):309–12. https://doi.org/10.1016/j.cirp.2018.04.101.
[8] Furushima T, Manabe K. Experimental study on multi-pass dieless drawing process of superplastic Zn-22%Al alloy microtubes. J Mater Process Technol 2007;187: 236–40. https://doi.org/10.1016/j.jmatprotec.2006.11.204.
[9] Milenin A, et al. *Improving the workability of materials during the dieless drawing processes by multi-pass incremental deformation.* Archives of civil and mechanical. Engineering 2020;20(3). https://doi.org/10.1007/s43452-020-00092-4.
[10] Braatz M, Bohlen J, Ben Khalifa N. Process stability and reproducibility of the Dieless drawing process for AZ31 magnesium wires. Key Eng Mater 2022;926: 389–400. https://doi.org/10.4028/p-lm7s8y.
[11] Nienaber M, et al. Property profile development during wire extrusion and wire drawing of magnesium alloys AZ31 and ZX10. Mater Des 2022:224. https://doi.org/10.1016/j.matdes.2022.111355.
[12] Tiernan P, Hillery MT. Dieless wire drawing - an experimental and numerical analysis. J Mater Process Technol 2004;155:1178–83. https://doi.org/10.1016/j.jmatprotec.2004.04.175.
[13] Tiernan P, Hillery MT. An analysis of wire manufacture using the dieless drawing method. J Manuf Process 2008;10(1):12–20. https://doi.org/10.1016/j.manpro.2008.05.001.
[14] Milenin A. Rheology-based approach of design the dieless drawing processes. Archives of Civil and Mechanical Engineering 2018;18(4):1309–17. https://doi.org/10.1016/j.acme.2018.04.003.
[15] Naughton MD, Tiernan P. Requirements of a dieless wire drawing system. J Mater Process Technol 2007;191(1–3):310–3. https://doi.org/10.1016/j.jmatprotec.2007.03.054.
[16] Seitz JM, et al. The manufacture of Resorbable suture material from magnesium – drawing and stranding of thin wires. Adv Eng Mater 2011;13(12):1087–95. https://doi.org/10.1002/adem.201100152.
[17] Mei D, et al. Corrosion behavior of mg wires for ureteral stent in artificial urine solution. Corros Sci 2021:189. https://doi.org/10.1016/j.corsci.2021.109567.
[18] Furushima T, Manabe K. Finite element simulation with coupled Thermo-mechanical analysis of superplastic Dieless tube drawing considering strain rate sensitivity. Mater Trans 2009;50(1):161–6. https://doi.org/10.2320/matertrans.P-MRA2008837.
[19] Fortunier R, Sassoulas H, Montheillet F. A thermo-mechanical analysis of stability in dieless wire drawing. Int J Mech Sci 1997;39(5):615–27. https://doi.org/10.1016/s0020-7403(96)00060-4.
[20] Pawelski O, Kolling A. Calculation of the temperature distribution in dieless drawing. Steel research 1995;66(2):50–4. https://doi.org/10.1002/srin.199501087.
[21] Weidig U, et al. Muliphase microstructure steel bars produced by dieless drawing. steel research 1999;70(4+5):172/77.
[22] Weidig U, Steinhoff K. Neue Perspektiven und Anwendungen für das frei Längen. In: Steinhoff K, Knopp R, editors. Umformtechnik im Spannungsfeld zwischen Plastomechanik und Werkstofftechnik. Bad Harburg: Grips media GmbH; 2008. p. 217–31.
[23] Braatz, M., J. Bohlen, and N. Ben Khalifa, Experimental and Numerical Investigation of the Forming Zone in Dieless Wire Drawing Process of Thin Biometallic Wires, in Proceedings of the 14th International Conference on the Technology of Plasticity - Current Trends in the Technology of Plasticity. 2024. p. 479–490, Doi:https://doi.org/10.1007/978-3-031-41023-9_49.
[24] Hongyu W, et al. Analysis and study of dieless drawing process for rod based on radial direction gradient slab method. Int J Adv Manuf Technol 2018;98(1–4): 839–47. https://doi.org/10.1007/s00170-018-2282-5.
[25] He Y, et al. Rectifying control of wire diameter during dieless drawing by a deformation measuring method of interframe displacement. Int J Miner Metall Mater 2012;19(7):615–21. https://doi.org/10.1007/s12613-012-0603-5.

[26] Braatz M, Bohlen J, Ben Khalifa N. Process window and mechanical properties for thin magnesium- and zinc-wires in dieless wire drawing. Int J Mater Form 2024;17 (5). https://doi.org/10.1007/s12289-024-01848-6.
[27] Cano-Castillo, G., et al., Effect of ca and Nd on the microstructural development during dynamic and static recrystallization of indirectly extruded mg–Zn based alloys. Mater Sci Eng A, 2020. **793**, Doi:https://doi.org/10.1016/j.msea.2020 .139527.
[28] Seitz J-M, et al. The manufacture of Resorbable suture material from magnesium. Adv Eng Mater 2010;12(11):1099–105. https://doi.org/10.1002/ adem.201000191.
[29] Nienaber M, et al. On the direct extrusion of magnesium wires from mg-Al-Zn series alloys. Metals 2020;10(9). https://doi.org/10.3390/met10091208.
[30] Máthis K, et al. The evolution of non-basal dislocations as a function of deformation temperature in pure magnesium determined by X-ray diffraction. Acta Mater 2004;52(10):2889–94. https://doi.org/10.1016/j.actamat.2004.02.034.
[31] Drury MR, Humphreys FJ, White SH. Large strain deformation studies using polycrystalline magnesium as a rock analogue. Part II: dynamic recrystallisation mechanisms at high temperatures. Phys Earth Planet Inter 1985;40(3):208–22. https://doi.org/10.1016/0031-9201(85)90131-1.
[32] Beer AG, Barnett MR. Influence of initial microstructure on the hot working flow stress of mg–3Al–1Zn. Mater Sci Eng A 2006;423(1–2):292–9. https://doi.org/ 10.1016/j.msea.2006.02.041.
[33] Cheng YQ, et al. Flow stress equation of AZ31 magnesium alloy sheet during warm tensile deformation. J Mater Process Technol 2008;208(1–3):29–34. https://doi. org/10.1016/j.jmatprotec.2007.12.095.
[34] Karimi E, et al. Instantaneous strain rate sensitivity of wrought AZ31 magnesium alloy. Mater Des 2013;49:173–80. https://doi.org/10.1016/j.matdes.2013.01.068.
[35] Naughton MD, Tiernan P. Theoretical analysis of heat transfer in dieless wire drawing. Int J Comput Mater Sci Surf Eng 2009;2(1/2). https://doi.org/10.1504/ ijcmsse.2009.024926.
[36] Zener C, Hollomon JH. Effect of strain rate upon plastic flow of steel. J Appl Phys 1944;15(1):22–32. https://doi.org/10.1063/1.1707363.
[37] Ryan ND, McQueen HJ. Dynamic softening mechanisms in 304 austenitic stainless steel. Can Metall Q 2013;29(2):147–62. https://doi.org/10.1179/ cmq.1990.29.2.147.
[38] Zhang L, et al. Constitutive model and recrystallization mechanism of mg-8.7Gd-4.18Y-0.42Zr magnesium alloy during hot deformation. Materials (Basel) 2022;15 (11). https://doi.org/10.3390/ma15113914.
[39] Ramberg W, Osgood WR. Description of stress-strain curves by three parameters. NASA; 1943.
[40] Schneider S, et al. Study of the non-linear stress-strain behavior in Ti-Nb-Zr alloys. Mater Res 2005;8(4):435–8. https://doi.org/10.1590/s1516-14392005000400013.
[41] Kammer C. Eigenschaften von reinem Magesium. In: Aluminium-Zentrale D, editor. Magnesium Taschenbuch. Düsseldorf: Aluminium-Verlag; 2000. p. 77–98.
[42] Lienhard, J.H.I. and J.H.V. Lienhard, A Heat Transfer Textbook. 2001: Phlogistron.